ATD: A Multiplatform for Semiautomatic 3-D Detection of Kidneys and Their Pathology in Real Time

Emmanouil Skounakis, Konstantinos Banitsas, Atta Badii, Stavros Tzoulakis, Emmanuel Maravelakis, and Antonios Konstantaras

Abstract—This research presents a novel multifunctional platform focusing on the clinical diagnosis of kidneys and their pathology (tumors, stones and cysts), using a "templates"-based technique. As a first step, specialist clinicians train the system by accurately annotating the kidneys and their abnormalities creating "3-D golden standard models." Then, medical technicians experimentally adjust rules and parameters (stored as "templates") for the integrated "automatic recognition framework" to achieve results which are closest to those of the clinicians. These parameters can later be used by nonexperts to achieve increased automation in the identification process. The system's functionality was tested on 20 MRI datasets (552 images), while the "automatic 3-D models" created were validated against the "3-D golden standard models." Results are promising as they yield an average accuracy of 97.2% in successfully identifying kidneys and 96.1% of their abnormalities thus outperforming existing methods both in accuracy and in processing time needed.

Index Terms—Abnormalities detection, automatic annotation, kidney, kidney pathology, kidney segmentation, region of interest (ROI), stone, tumor.

I. INTRODUCTION

The rapid evolution of advanced medical image modalities such as the modern MRI scanners and the large amount of data provided have brought about the need for more automatic processes in computer-aided diagnosis. Clinicians need to examine large numbers of complex medical images to detect abnormalities; a difficult and time consuming task. Hence, there is a need for systems that will automatically detect organs and their possible abnormalities and provide useful metrics.

Several algorithms detect kidney abnormalities, addressing the challenge of increased difficulty in their delineation due to their intensity variation. Prevost *et al.* [1] had automatically localized the kidney with a novel ellipsoid detector, and then applied deformation of this ellipsoid with a model-based approach in the segmentation process. Using the Dice Similarity Coefficient (DSC) as a metric [2], this system achieved a DSC of 87.5%. Similar to this platform, they calculated the accuracy of automatic segmentation outcome by comparing it with the result of the semiautomatic segmentation method coming from the radiologist's work (golden standard). Lin *et al.*'s [3] model-based approach for kidney segmentation achieved an average correlation coefficient of 88%,

while [4] used Bayesian concepts for a probability map generation to achieve an automatic kidney Parenchyma volumetry with a DSC of 90.3%. [5] used an automated graph-cuts segmentation technique for dynamic contrast-enhanced 3-D MR renography achieving a DSC of 96% for the kidney and 90% for the cortex and the medulla. Their method was very fast (approximately 20 min) compared with the time needed for a manual segmentation of about 2.5 h, In [6], the authors presented a combination of texture features and a statistical matching of geometrical shapes of kidneys for an automatic segmentation in 3-D MRI images with a mean DSC of 90.6%.

Concerning abnormality detection, [7] presented a finite-element method based on 3-D tumor growth prediction for kidney tumors, with an average true positive fraction of 91.4% on all tumors. Tamilselvi and Thangaraj [8] used an improved seeded region growing method and classification of kidney images with stones and focused on the kidney image segmentation and diagnosis for stone detection. In [8] the authors achieved a DSC of 95%. In [9] three neural network algorithms for diagnosis of kidney stones diseases were tested. They claim that the multilayer perception with two hidden layers and the back propagation algorithm produced the best model for the diagnosis of kidney stone disease with an accuracy of 92%. In [10], an automatic segmentation algorithm for segmenting liver and tumor based on threshold and region growing techniques was used. The tumor was segmented with an alternative FCM clustering algorithm and the DSC for liver and tumor was 95.8% and 89.8%, respectively. The methodology of [11] was closer to the one presented here as their automatic segmentation method was based on association rule-mining to enhance the diagnosis and classification of kidney images. They used conditions and criteria to adjust their system, thus achieving results with an average accuracy of 92%.

In [14] a survey of systems focusing on identifying pathologies in transplanted kidneys with most of those methods suffering from low accuracy, or the need for extended involvement of clinicians to identify organs and abnormalities was presented. In the field of transplant kidney rejection, [12] and [13] presented a related system based on dynamically enhancing the contrast of 2-D MRI images with achieve organ identification. The first part of their method is related to our own system and achieved an average accuracy of 92.31% (although our system focuses on tumor detection as well as generic abnormalities).

This research presents the automatic tumor detection (ATD) platform; an innovative system to support a method for increased automation of kidney detection as well as their abnormalities (tumors, stones, and cysts). This system uses a novel approach to increase both the accuracy and the automation of the process. Initially, a clinician invokes a fast version of the region growing segmentation algorithm and a set of advanced correction tools to semiautomatically detect and annotate the regions of interest (RoI), and to annotate the organs and their potential abnormalities (tumors, stones and cysts) in a specific MRI dataset. Next, a medical technician defines the rules and parameters for the automatic recognition framework and thus generates 3-D models of the organs and their potential pathology similar to the ones defined by the clinicians. This produces a "template" that includes all the "sensitivity" parameters that govern the dataset that come from a specifically calibrated MRI. The final step is for any user to apply this template's settings to all other datasets of the same type and automatically identify the organs and their dysfunctions.

This semiautomatic tumor detection system has a number of advantages over the existing systems given as follows:

1) ATD is not only a method, but a multifunctional platform supporting real-time processing;
2) it simultaneously detects organs as well as their pathology (tumors, stones and cysts) with increased accuracy;
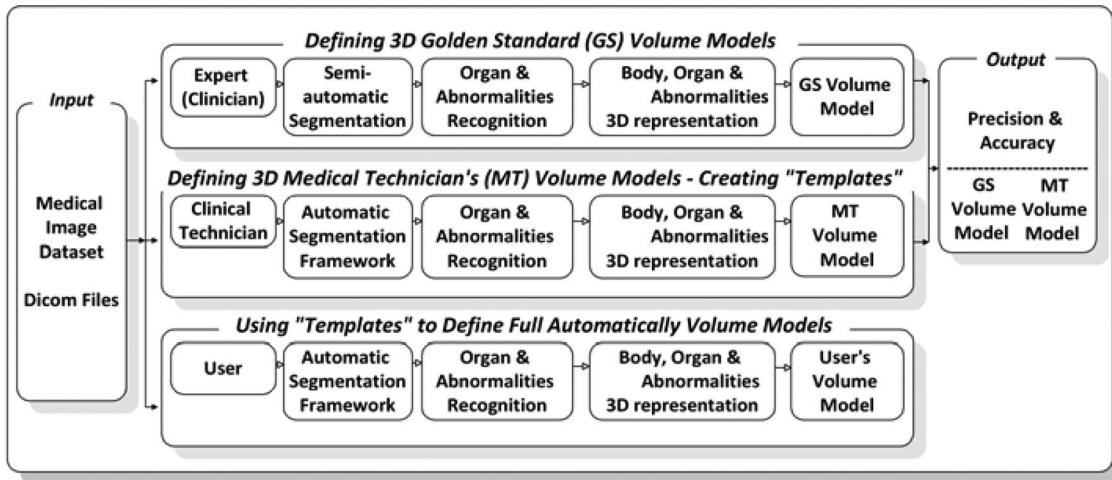
Fig. 1. Methodology used for the evaluation of the automatic segmentation framework Clinician's [or Golden Standard (GS)] Volume Model versus the Medical Technician's (MT) Volume Model.

3) processing time is faster than the existing methods, as the main algorithms and additional controls run "on the fly." The processing time for a 24 slices MRI dataset is about 1 min;

4) a novel mechanism for the seed pixel method avoids selection of irrelevant isolated pixels (implementing a top-down connectivity analysis between slices);

5) the system achieves more accurate results for the recognition of kidneys compared with the existing methods by implementing additional controls.

The platform also supports storage of information in small anonymous xml-structured files (with a 500-kbytes typical file size for a complete dataset) to ensure fast transmission via networks to other clinicians. A typical size of a "template" file is about 2 kbytes.

II. METHODOLOGY

The method for creating and validating outputs of the ATD platform consists of three steps (see Fig. 1).

A. Defining "Three- Dimensional Golden Standard Models"

The process calls for clinicians to annotate organs and pathologies in an abdominal MRI dataset in order to define a "golden standard model" for the evaluation. For this process the "manual segmentation panel" integrates an advanced implementation of the "region-growing" semiautomatic segmentation algorithm.

Boundary refinement can be achieved by using a custom version of the "pencil" and "eraser" tools (keeping their neighboring points connected) allowing for the expansion or shrinkage of the selected areas so as to add or remove any mistakenly selected or ignored areas.

The integrated multilevel multifunctional annotation system facilitates the delineation of areas of interest in the selected image. Once the delineation process has been completed, the "3-D volume rendering" option creates and enables the manipulation of the resulting realistic 3-D model of the organ structure and its potential abnormalities.

The implementation uses "visualization toolkit" (VTK) [16], with visualization algorithms in a 3-D interactive process (Fig. 2). Seven different views of the 3-D model are available along with corresponding metrics (see Fig. 2 left side). They include MIP. (pH-sensitive Molecularly Imprinted Polymer), composite ramp, composite shade ramp, skin, bone, muscle and RGB composite. Newer volume rendering methods are in development [17], [18].

B. Creating Templates With Rules and Parameters to Identify Specific Areas of Interest

By experimenting with the parameters of the "automatic region-oriented segmentation framework," a medical technician attempts to achieve a segmentation result closest to that of the clinician's using a region-oriented segmentation method [15]. A panel enables the interactive adjustment of the parameters of the framework in a single slide and the checking of the corresponding result in real time.

Once the result is acceptable, the parameters and rules can be saved in a "template" with a name that corresponds to the area identified (e.g., right kidney) and can then be applied automatically to the entire image dataset. For highly complex images, the clinician has the option to define a "working area" where the Framework will be applied (see Fig. 3).

The "validation" panel allows an evaluation by comparing the results for the two models for every slide. This panel shows the "true positives" pixels which are the common pixels in the two methods (orange), the "false negatives" pixels which are presented only in the clinician's work (blue) and the "false positives" pixels which are presented only in the second image produced by the automatic method (green).

C. Using Existing Templates for Fully Automatic Identification of Specific Areas of Interest

An end user can employ the existing "templates" to find a specific organ (e.g., left Kidney) and its potential abnormalities. The location of the organs can vary from one dataset to another; to identify the initial position of the organ, the engineer loads the "template" in any of the images including that organ and then clicks to verify the already selected organ from a list of objects.

The system's functionality was tested on a dataset of 20 MRIs (522 images) acquired at a local regional hospital and with the following parameters: the MRI machine was a GE Medical Systems, running a scanning sequence of SE and a variant of SK. The slice thickness was 8 mm with a repetition time of 2000 ms. Image frequency was 63.830539 MHz, magnetic field strength was 1.5 T, and spacing between slices was 10 mm.

A video displaying the segmentation techniques along with a demonstration of the user interface and a working copy of the platform is available at: www.creteportal.gr/ATDSegmentation.zip

Fig. 2.   3-D model of the body integrating the previously delineated areas. Green represents the kidneys, while red identifies the tumor.

Fig. 3.   Defining parameters and rules ("Templates") for the automatic segmentation process.

III. SEGMENTATION ALGORITHMS

The "segmentation framework" is responsible for the training of the systems as well as the creation of the "templates." The basic steps of this framework are as follows.

1) A clinician opens an MRI dataset (i.e., abdominal).
2) An edge-preserving anisotropic diffusion filter (Perona-Malik) removes the noise of the images [20].
3) The clinician selects the RoI, the organ, and the abnormalities and saves these choices.
4) Later, a medical technician defines the working area thus reducing the amount of data to be processed.
5) A modified version of a region-oriented segmentation algorithm is introduced to recognize the organs [15]. The histogram val-

ues are normalized to get better results: the user interactively defines the parameters to smooth the histogram (the up/down values to recognize more or less compact internal areas and the area parameter to avoid selecting tiny objects during the organ's recognition process).

6) The value of the seed pixel and the sensitivity are defined and used for the recognition of abnormalities.
7) The medical technician records the best results and then stores the generated values into a "template."
8) Another user can now get a dataset of the same type (e.g., abdominal) and select a template to identify specific organs (e.g., kidneys). The framework will automatically define the organ in the dataset and detect the potential abnormalities.

9) Next, the key processes of the above steps are detailed.

A. Region Growing Semiautomatic Segmentation Algorithm

Starting from a seed pixel, the algorithm finds and demarcates structures as a mass of neighboring pixels in image areas. It examines the intensity levels of the neighboring pixels and recruits them as belonging to the structure being grown by spreading the selection outward starting from a predefined seed pixel whose gray-level intensity value, plus/minus a so-called "tolerance value," forms the reference value for such recruitment of similar pixels [19].

The ATD platform integrates an enhanced version of this algorithm, to speed up the segmentation task:

1) a slider allows the adjustment of the tolerance value interactively for the selection of the desired area in the image, just after the "start point" selection;
2) an image mask (matrix) speeds up the segmentation process by ensuring that pixels already examined will not be checked again.

To solve the problem with the fuzzy transition zones at the boundaries of the designated areas of interest (e.g., kidney), advanced versions of the pencil and eraser correction tools are integrated in the platform (working with areas and not with pixels), to automatically keep the similar neighboring points connected, providing clinicians with the option to swiftly refine their delineations.

B. Region Oriented Segmentation Framework

In order to support automation of the diagnosis process, the proposed segmentation framework has 5 steps as follows.

1) Preprocessing: The segmentation process starts with a preprocessing procedure using an edge-preserving anisotropic diffusion filter [20], so that small image artifacts are smoothed (intraregional smoothing), while objects of interest such as edges are enhanced (inhibiting inter-regional smoothing).

2) Rules Definition: Using a modified region-oriented segmentation algorithm [15], the user can define a region of interest to minimize the image information to be processed. Where there is no such definition of a working area where the organ is located, the automatic process would typically result in a larger number of areas being recognized as objects of interest. Defined "working areas" are also stored in "templates."

3) Parameters Definition: In (1), the key parameters of the image are defined: $h(gv)$ is the histogram value for a specific gray-scale value gv, Max is the maximum value of the histogram, and NormMax is the normalized maximum value defined by the user.

$$h(gv) = \text{int}((\text{float})h(gv) * \text{NormMax}/\text{Max}). \qquad (1)$$

To identify the abnormalities located in a designated area, the histogram entries have to be compressed in such a way that the lower entries of the histogram are emphasized. This is achieved by using (2).

$$h(gv) = 10\sqrt{h(gv)}. \qquad (2)$$

In this way, small peaks in the histogram corresponding to small areas in the image are emphasized, allowing the algorithm to detect them more accurately.

A process of smoothing the histogram must also be applied to homogenize and successfully detect relatively large areas (organs) avoiding the insignificant local peaks (i.e., variations in luminance inside the organ's image area). The histogram is smoothed by applying the computational method whereby all the intensity values of the pixels in the image are recalculated by determining the average of a predefined number of neighboring pixels of the histogram. This interpolation
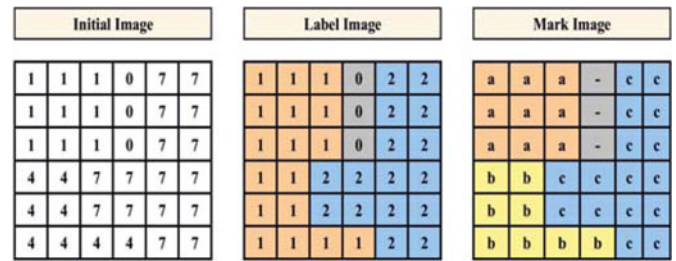

Fig. 4.   Automatic identification of objects using L-shaped masks (3 Objects a, b, and c are identified).

"width" parameter is defined experimentally and interactively by the user. Higher "width" values are associated with larger areas being designated as part of the organ structure of interest, while low width values help the user pick out the smaller structures thus attempting to avoid missing any important parts of the image. The detection of the falling and rising histogram edges determines the number of valleys in the histogram, thus inferring the threshold values (Lm):

$$\text{Lm} = a + \text{down} + [b - (a + \text{down})]/2. \qquad (3)$$

In this equation, a represents a local maximum value, and b is the point where the histogram starts to rise again (ignoring any small peaks under a predefined limit value). These local minimum values (Lm) are used to segment objects and to create a "label image." The closer the peak of this curve is to Lm, the more the delineated boundary moves inwards toward the center of the kidney.

The platform provides the clinician with the option to define the "up" and "down" parameters which are also stored in the "templates" in order to achieve the desired Lm values in complex images.

Finally, applying any filter to an image introduces a certain amount of noise. This noise is removed with 3×3 erosion-dilation linear morphological filters.

4) Connectivity Analysis: In order to create the final "mark image" which depicts the regions of interest, L-shape masks (based on a six-connected neighborhood technique) are used [21] to compare the label value of every pixel with the values of the neighboring pixels (see Fig. 4). The pixels with the same values in the "label image" but different values in the "initial image" are included in the list of pixels to be considered later when identifying the number of the different objects in the image.

In this example, the "mark image" contains four identified regions. This is based on the work of Bassmann and Besslich [15] which sets out this method in detail.

The modifications applied to the "fully automatic region-oriented segmentation framework" include the addition of a preprocessing filtering procedure [20], (2) to emphasize the details of the current type of images (e.g. abdominal), an implementation of an L-shape mask based on the six-connected neighborhood pixels in the connectivity analysis (CA) process, and a top-down connectivity analysis of the detected regions. The CA method requires the calculation of the average intensity of the gray-level values of the selected region and the definition of a tolerance value as well as at least ten common points between one image slide and the next so as to verify the region boundary and detect the desired region successfully.

5) Features: The proposed segmentation framework applied to an abdominal MRI dataset can delineate RoIs which can be categorized based on features such as the compactness, the center of gravity (the central point of a defined area), total area (number of the pixels), and the perimeter of a specific region. The compactness and the center of
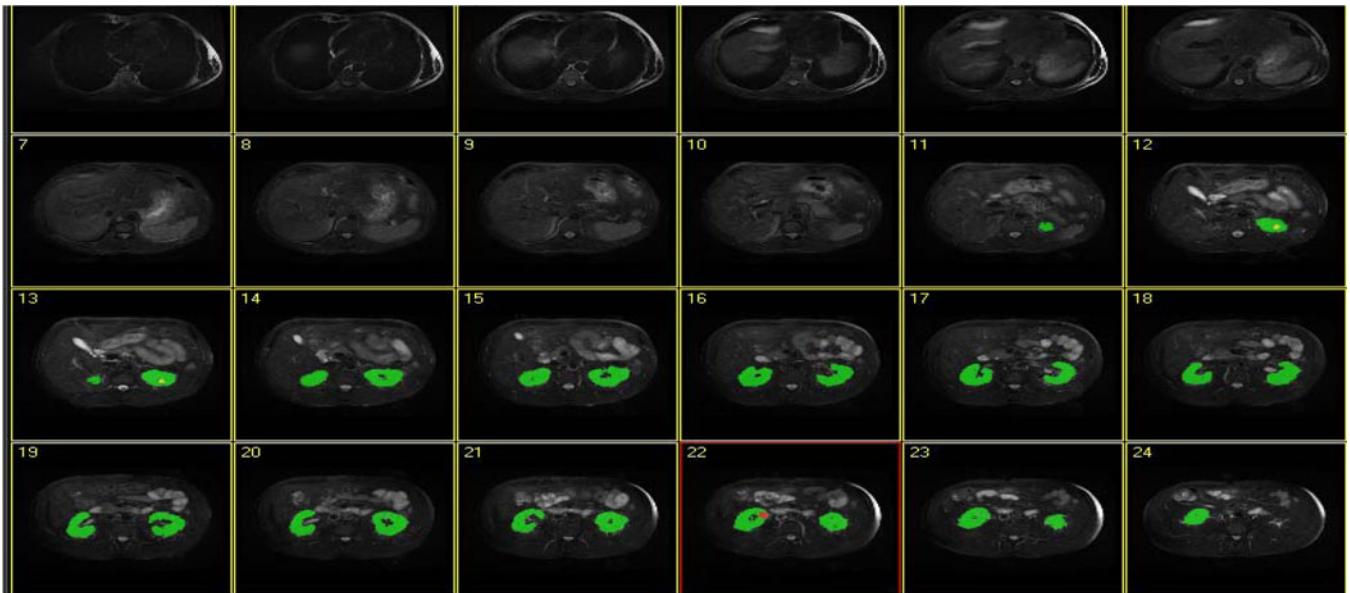
Fig. 5.   Automatic identification of objects (e.g. "Left Kidney," "Right Kidney," "Right Kidney Tumor" (No 22 slide), and "Left Kidney Stone" (No 12 and No 13 slides) – SE00004 MRI dataset).

gravity are features that are independent of the exact position, rotation and scaling of the object; therefore, they are very useful in the identification process.

The current version of the system stores another two parameters in the "template" file. First, the "area" which is a criterion to be considered so as to avoid detecting very small objects during the organ identification process, and second, the "center of gravity" of an object which must be located in the working area and must encompass all the pixels of the object.

For the recognition of kidney abnormalities (tumors, stones and cysts), some statistical data are additionally considered to arrive at the threshold values for the average gray-level intensity typical of some structures representing abnormal or pathological changes.

Cysts are relatively dark; tumors are grey, while stones have relatively higher gray-level values. The "analysis" panel enables the medical technician to experiment and define three parameters for the identification of any of the aforementioned pathologies consistent with the clinician's judgment. The first parameter refers to the gray-level "value" that the pixels of an object are expected to have to be designated as such, e.g., recognized as a stone, a tumor, or a cyst. Due to the nonhomogenous distribution of gray-level values of the pixels of such organs, a "tolerance" value must also be defined so that "gray-level Value ± Tolerance" corresponds to the range of intensities of pixel values typically expected to depict such abnormal structures. In this way, pixels which meet the above criteria are obtained.

However, this methodology can also erroneously designate a number of irrelevant pixels with similar intensities scattered in the organ image (classification noise). To identify the best candidate seeds corresponding to the abnormalities and thus minimize the classification noise, a 5×5 erosion filter is used. During this process, the medical technician must declare the number of neighborhood pixels (threshold) to be taken into account (Maximum $5 \times 5 = 25 - 1 = 24$ neighborhood pixels).

Finally, the best candidate seeds with intensity levels closest to the respective thresholds are used in the filling process (region growing) to demarcate the substructural areas which represent kidney abnormalities.

IV. RESULTS

Evaluation of the "automatic segmentation framework," which is integrated in the ATD platform, is based on the following five criteria [22].

1) *Accuracy,* the proportion of true results ("True Positives" and "True Negatives") in the total population of the results.
2) *Precision,* the proportion of "True Positives" against all the positive results ("True Positives" and "False Positives").
3) *Sensitivity,* the ability of the system to identify positive results. It measures the proportion of positives which are correctly identified as such.
4) *Specificity*, the ability of the system to identify negative results, meaning that it measures the proportion of negatives correctly identified as such.
5) DSC, defines the similarity measure over two 3-D volume models (here GS which is the Clinician's Golden Standard volume model versus MT which is the Medical Technician's volume model).

Although a medical technician is involved in this process, his/her subjective opinion has very little effect on the overall process. Once the process is finished, the automatic results are compared with the output of the clinician's work. Therefore, any misguided selection performed by the medical technician will be cancelled out, since the main 3-D model of the findings has been initially defined by the clinician.

The average success rate for kidney detection is 97.2% and their abnormalities 96.1% respectfully (see Table IV). As an example of the method the following results were obtained (see Fig. 5 and Tables I, II and III) from a random MRI dataset (SE00004):

V. DISCUSSION

The proposed platform can achieve a highly accurate and fast identification of the kidneys, while being able to correctly identify any potential abnormalities (tumors, stones, and cysts) within the same platform. Overall, this platform supports the following features:
1) a multi-functional easy-to-use annotation system;

TABLE I
MRI DATASET EXAMPLE (SE000004), DELINEATION OF THE "LEFT KIDNEY"

No.	SE000004 MRI Dataset	True Positives (Correctly Selected)	True Negatives (Correctly Rejected)	False Positives (Mistakenly Selected)	False Negatives (Mistakenly Rejected)	Accuracy	Precision	Sensitivity	Specificity	Dice similarity
1	MR000000	0	262144	0	0					
2	MR000001	0	262144	0	0					
3	MR000002	0	262144	0	0					
4	MR000003	0	262144	0	0					
5	MR000004	0	262144	0	0					
6	MR000005	0	262144	0	0					
7	MR000006	0	262144	0	0					
8	MR000007	0	262144	0	0					
9	MR000008	0	262144	0	0					
10	MR000009	0	262144	0	0					
11	MR000010	651	261493	47	43	99.97%	93.27%	93.80%	99.98%	93.53%
12	MR000011	2238	259906	26	118	99.95%	98.85%	94.99%	99.99%	96.88%
13	MR000012	3254	258890	12	258	99.90%	99.63%	92.65%	100.00%	96.02%
14	MR000013	4225	257919	72	120	99.93%	98.32%	97.24%	99.97%	97.78%
15	MR000014	3954	258190	8	208	99.92%	99.80%	95.00%	100.00%	97.34%
16	MR000015	3727	258417	21	201	99.92%	99.44%	94.88%	99.99%	97.11%
17	MR000016	3472	258672	13	108	99.95%	99.63%	96.88%	99.99%	98.29%
18	MR000017	3603	258541	32	239	99.90%	99.12%	93.78%	99.99%	96.38%
19	MR000018	4250	257894	112	160	99.00%	97.43%	96.37%	99.96%	96.90%
20	MR000019	4408	257736	148	107	99.90%	97.65%	97.63%	99.94%	97.19%
21	MR000020	4018	258126	120	91	99.92%	97.10%	97.79%	99.95%	97.44%
22	MR000021	3021	259123	109	53	99.94%	96.52%	98.28%	99.96%	97.39%
23	MR000022	1850	260294	115	74	99.93%	94.15%	96.15%	99.96%	95.14%
24	MR000023	0	262144	0	0					
					Average	99.92%	97.69%	95.81%	99.98%	96.72%

TABLE II
DELINEATION OF THE "LEFT KIDNEY TUMOR" (SE000004 MRI DATASET)

No.	SE000004 MRI Dataset	True Positives (Correctly Selected)	True Negatives (Correctly Rejected)	False Positives (Mistakenly Selected)	False Negatives (Mistakenly Rejected)	Accuracy	Precision	Sensitivity	Specificity	Dice similarity
22	MR000021	349	262144	26	0	99.99%	93.07%	100.00%	99.99%	96.41%
					Average	99.99%	93.07%	100.00%	99.99%	96.41%

TABLE III
MRI DATASET EXAMPLE (SE000004), DELINEATION OF THE "LEFT KIDNEY STONE"

No.	SE000004 MRI Dataset	True Positives (Correctly Selected)	True Negatives (Correctly Rejected)	False Positives (Mistakenly Selected)	False Negatives (Mistakenly Rejected)	Accuracy	Precision	Sensitivity	Specificity	Dice similarity
12	MR000011	184	262144	13	0	100.00%	93.40%	100.00%	100.00%	96.59%
13	MR000012	171	262144	9	0	100.00%	95.00%	100.00%	100.00%	97.44%
					Average	100.00%	94.20%	100.00%	100.00%	97.01%

TABLE IV
KIDNEYS AND THEIR POTENTIAL PATHOLOGY DETECTION ACCURACY (DSC) IN EACH OF THE 20 MRI DATASETS

DSC	Total %	20 MRI Datasets - 552 Dicom Images																			
		1	2	3	4	5	6	7	8	9	10	11	12	13	14	15	16	17	18	19	20
Kidneys Detection	97.20	99	96	96	99	96	97	96	97	95	97	99	99	97	98	97	95	97	97	98	99
Kidneys Pathology Detection	96.10	94	96	96	95	95	96	94	97	96	96	98	96	98	97	96	97	95	99	96	95

TABLE V
AVERAGE TIMES TAKEN FOR SEMIAUTOMATIC AND FULLY AUTOMATIC SEGMENTATION OF KIDNEYS AND THEIR POTENTIAL DYSFUNCTIONS

(20 MRI Datasets - 552 Dicom Images, Average Times) Stages	Segmentation Methodology	
	Semi-automatic	Fully Automatic
Input of a Single Medical Image MRI Dataset (Average number 28 Images)	9.47 secs	9.47 secs
Load annotations	1.87 secs	1.87 secs
Kidney Segmentation	4 mins 54 secs	55 secs
Segmentation of Dysfunctions (Tumors, Stones and Cysts)	5 mins 55 secs	
Save Annotations	1.4 secs	1.4 secs
Save Template's parameters	0	0.5 secs
Total Time	11 mins 2 secs	1 min 8 secs

2) the ability for real-time detection of kidneys and their abnormalities (tumors, stones, and cysts);

3) a multi functional 3-D visualization system providing real size measurements;

4) evaluation of the results based on five measurement methods including a 3-D volumetric method.

After the initial development, the system was tested by clinicians and their feedback was used to improve the usability of the system. Clinicians commented favorably on the speed and accuracy of the system.

The clinicians expressed that as the system was able to recognize kidneys and any abnormal tissue located within them, it may be able to detect any abnormal tissue present in the surrounding areas. This is a desirable function, particularly if there is already clinical evidence of abnormal tissue within the organ.

The system is currently able to accurately detect "relatively compact" regions such as stones, cysts, and tumors in abdominal MRI datasets produced by well-calibrated MRI scanners. In more complex cases where, for example, a tumor has spread into different areas with varying intensities, the system can recognize the tumors with a decreased accuracy; this is currently being addressed through a set of more advanced algorithmic approaches under development.

Concerning the applicability of the work on different patients and in the case of using another MRI scanner for the same type of images (e.g., abdominal), the medical technician must readjust the "template" to achieve accurate results, as not all medical image modalities are calibrated in the same way. This calls for calibration of the sensitivity parameters on the platform (Width, Ascending, and Descending, Threshold and Area as explained in the text below), for more accurate delineations.

In order to deal with the possible inhomogeneity of images used, the platform performs the following steps.

1) The Region of Interest is defined.

2) The parameters used to accurately find the organ and its boundaries are defined: Width (for smoothing the histogram and get the correct boundaries of the organ), ascending and descending (for identifying local minimums), threshold (for removing the noise from the use of erosion—dilation morphological filters) and area (for initial identification of the organ ignoring tiny areas).

3) The parameters to find the correct seeds for the pathology detection to feed to the region growing algorithm are also defined: Grayscale and a tolerance value for the range of values to represent a dysfunction, as well as a threshold value for the erosion filter used to change the sensitivity governing the discard of seeds that are not strong enough.

By doing the above, the "framework" remains highly immune to datasets coming from different patients and even from different pathologies.

Finally, the output files were made anonymous and were also of a small size and thus easier to upload. This would also enable the system to securely and efficiently transmit files, including images, to client applications running on smartphones, so that clinicians and consultants could view the results on the move.

VI. Conclusion

This research presents a new MRI diagnosis-assistive platform that, after initial creation of a "template," is capable of providing a more automatic 3-D identification of kidneys and their abnormalities (tumors, stones, and cysts).

Two methods have been integrated to create "3-D volume models": The first provides clinicians with support (through a user interface) in order to rapidly identify and delineate areas of interest, with a 3-D view and have real metrics at hand specifying actual physical sizes of organ structures and any abnormal tissue regions. The second invokes a method of increased automation, to identify important areas based on "templates" that are initially created by a medical technician and later on used by a user with no particular prior knowledge of medical image segmentation. These "templates" allow the system to identify organ structures based on their features and look for any abnormalities.

Clinicians who participated in the trials expressed satisfaction with the use of the platform in that it offered better visualization of regions of interest, as it simplified and sped up the image annotation process even in very complex medical image datasets, enabling higher accuracy in organ and abnormality identification.

As using the system requires no previous knowledge of autolabeling, it is easy to support the clinical diagnosis process throughout; from the input stage of the MRI image datasets, to the generation of 3-D models. The fully automated part of the framework (after the creation of "templates") has been tested on 20 MRI datasets corresponding to an equal number of patients (552 Images).

Benchmarking tests of the system have shown promising results. For the recognition of kidneys and their abnormalities, the system outperformed previously reported results with a mean DSC of 97.2% and 96.1%, respectively, compared with other systems with a mean DSC 95% and 91%.

Apart from being accurate, the automatic mode is notably faster compared with any existing method to date for the automatic recognition of the kidneys, while it is also the first platform that simultaneously identifies abnormalities in the organ's area such as tumors, stones, and cysts (Table V).

In the next revision of the system, the capability for the transmission of selected compressed images to a mobile device or smartphone will be added. This will allow clinicians to receive such clinical information and offer opinions while they are on the move.

References

[1] R. Prevost, B. Mory, J. Correas, L. D. Cohen, and R. Ardon, "Kidney detection and real-time segmentation in 3D contrast-enhanced ultrasound images," in *Proc. 9th IEEE Int. Symp. Biomed. Imag. ISBI*, Barcelona, Spain, 2012, pp. 1559–1562.

[2] K. H. Zou *et al.*, "Statistical validation of image segmentation quality based on a spatial overlap index," *Academic Radiol.*, vol. 11, no. 2, pp. 178–189, Feb. 2004.

[3] D. T. Lin, C. C. Lei, and S. W. Hung, "Computer-aided kidney segmentation on abdominal CT images," *IEEE Trans. Inform. Tech. Biomed.*, vol. 10, no. 1, pp. 59–65, Jan. 2006.

[4] O. Gloger, K. D. Tonnies, V. Liebscher, B. Kugelmann, R. Laqua, and H. Volzke, "Prior shape level set segmentation on multistep generated probability maps of MR datasets for fully automatic kidney parenchyma volumetry," *IEEE Trans. Med. Imag.*, vol. 31, no. 2, pp. 312–325, Feb. 2012.

[5] H. Rusinek, Y. Boykov, M. Kaur, S. Wong, L. Bokacheva, J. B. Sajous, A. J. Huang, S. Heller, and V. S. Lee, "Performance of an automated segmentation algorithm for 3-D MR renography," *Magn. Resonance Med.*, vol. 57, pp. 1159–1167, 2007.

[6] H. Akbari and B. Fei, "Automatic 3D segmentation of the kidney in MR images using wavelet feature extraction and probability shape model," *Med. Imag., Image Process.*, vol. 8314, pp. 83143D1–83143D7, Feb. 2012.

[7] X. Chen, R. Summers, and J. Yao, "FEM-based 3-D tumor growth prediction for kidney tumor," *IEEE Trans. Biomed. Eng.*, vol. 58, no. 3, pp. 463–467, Mar. 2011.

[8] P. R. Tamilselvi and P. Thangaraj, "Computer aided diagnosis system for stone detection and early detection of kidney stones," *J. Comput. Sci.*, vol. 7, no. 2, pp. 250–254, 2011.

[9] K. Kumar and B. Abhishek, "Artificial neural networks for diagnosis of kidney stones disease," *I. J. Inf. Technol. Comput. Sci.*, vol. 7, pp. 20–25, 2012.

[10] S. S. Kumar, R. S. Moni, and J. Rajeesh, "Automatic segmentation of liver and tumor for CAD of liver," *J. Advances inf. technol.*, vol. 2, no. 1, pp. 63–70, Feb. 2011.

[11] J. S. Jose, R. Sivakami, N. U. Maheswari, and R. Venkatesh, "An efficient diagnosis of kidney images using association rules," *Int. J. Comput. Technol. Electron. Eng.*, vol. 12, no. 2, pp. 14–20, 2012.

[12] F. Khalifa, A. El-Baz, G. Gimel'farb, and M. Abu El-Ghar, "Non-invasive image-based approach for early detection of acute renal rejection," in *Proc. Mid. Image Comput. Comput.-Assisted Intervention Conf. 2010*, 2010, pp. 10–18.

[13] F. Khalifa, M. A. Ghar, and T. Diasty, "Dynamic contrast-enhanced MRI-based early detection of acute renal transplant rejection," *IEEE Trans. Med. Imag.*, vol. 32, no. 10, Oct. 2013.

[14] M. Mostapha *et al.*, "Dynamic MRI-based computer diagnostic systems for early detection of kidney transplant rejection: A survey," presented at the Amer. Inst. Phys. Conf. Proc., Sydney, Australia, vol. 1559, pp. 297–306, Nov. 27–29, 2013.

[15] H. Bassman and P. W. Besslich, *Ad Oculos Digital Image Processing Student Version 2.0*. London, U,K.: International Thomson Publishing, 1995, pp. 117–152.

[16] The Visualization Toolkit (VTK). (Oct. 2013). [Online]. Available: http://www.vtk.org/.

[17] M. Hadwiger, C. Berger, and H. Hauser, "High-quality two-level volume rendering of segmented data sets on consumer graphics hardware," in *Proc. IEEE Vis.*, Oct. 24, 2003, pp. 301–308.

[18] D. Xiang, Tian, Jie, F. Yang, and Q. Yang, "Skeleton cuts—An efficient segmentation method for volume rendering," *IEEE Trans. Vis. Comput. Graph.*, vol. 17, no. 9, pp. 1295–1306, Sep. 2011.

[19] H. Fujita and M. Fejri, "New trends in software methodologies, tools and techniques: How to create the magic wand?" in *Proc. 5th SoMeT-06*, 2006, pp. 127–132.

[20] P. Perona and J. Malik, "Scale-space and edge detection using anisotropic diffusion," *IEEE Trans. Pattern Anal. Mach. Intell.*, vol. 12, no. 7, pp. 629–639, Jul. 1990.

[21] B. K. P. Horn, *Robot vision*. Cambridge, MA, USA: MIT Press, 1986.

[22] T. Mahalakshmi, B. L. Aswathi, and A. S. Nair, "Connectivity characteristic of transcription factor," *Int. J. Inf. Commun. Eng. World Academy Sci. Eng. Technol.*, vol. 5, no. 7, pp. 471–474, 2009.